Journal of Structural Geology 56 (2013) 34–44

Contents lists available at ScienceDirect

Journal of Structural Geology

journal homepage: www.elsevier.com/locate/jsg

Weathering history of an exposed bedrock fault surface interpreted from its topography

Zhanyu Wei, Honglin He*, Feng shi

Key Laboratory of Active Tectonics and Volcano, Institute of Geology, China Earthquake Administration, Beijing 100029, China

ARTICLE INFO

Article history:
Received 19 January 2013
Received in revised form
11 August 2013
Accepted 22 August 2013
Available online 30 August 2013

Keywords:
Bedrock fault surface
Weathering
Roughness
Faulting

ABSTRACT

Morphologic features of bedrock fault scarps are underutilized in studying faulting and weathering history, partly because of a lack of accurate quantitative parameters for topography. The study employs ground-based LiDAR to measure five patches at different levels on the same fault surface and then calculates roughness in the form of power spectral density in directions parallel and perpendicular to the slip. The power spectral density and spatial frequency typically follow a power law for each fault patch, showing approximately linear relationships in a log–log plot. However, due to additional power introduced by weathering, all spectral curves, especially those parallel to the slip, can be divided into two segments, lower-frequency (wavelengths of several centimeters – several meters) and higher-frequency (wavelengths of several centimeters and below) domains. This shows that the topographic features at different spatial scales are dominated by different mechanical processes: faulting abrasion in the lower-frequency domain and the weathering process in the higher-frequency domain. Moreover, we develop two parameters to quantify the degree of weathering of a fault outcrop, which is significant to describe the evolution of the fault-scarp and infer the date of faulting under calibration.

1. Introduction

A fault scarp is an important specific tectonic landform caused by faulting, either in unconsolidated sediments or in bedrock. The morphology of the fault scarp in unconsolidated sediments could be used to establish faulting history by a diffusion model (Andrews and Hanks, 1985; Nash, 1986; Arrowsmith et al., 1998), whereas a bedrock fault scarp does not evolve in the same predictable, time-dependent fashion as an equivalent scarp in unconsolidated sediments. As a result, a bedrock scarp is not considered a sensitive indicator of the timing and magnitude of past faulting events (Mayer, 1984; Stewart, 1993). However, other researchers have reported paleoseismological implications of bedrock fault scarps and described their morphologies in an attempt to extract useful information concerning earthquake recurrence intervals. For example, Wallace (1984) and Stewart (1996) delimited the slip increment of every faulting event by identifying different parallel weathered bands on exposed fault planes. Giaccio et al. (2002) made use of image processing and roughness analysis of an exposed bedrock fault surface as a paleoseismological analysis tool in the Campo Felic fault. In the last several years, bedrock fault scarps have become an attractive alternative for paleoseismological studies because the exposure duration of a bedrock fault scarp can be determined directly by methods based on the accumulation of cosmogenic nuclides (Zreda and Noller, 1998; Benedetti et al., 2000; Mitchell et al., 2001). The dating result of cosmogenic nuclides close to the bedrock fault surface may, however, have an ambiguous interpretation of faulting history due to interference from the surroundings and the weathering of the bedrock fault surface, and the ambiguity may be identified through the combination of a micro-morphologic analysis of the exposed fault scarps (Mitchell et al., 2001).

For some time geologists have noted that the surface of rocks vary systematically in their weathering characteristics, and have developed methods to estimate exposure time based on progressive and time-dependent changes of rock surface morphology (Birkeland and Noller, 2000), such as the statistics of erosion and lichen pitting (Burke and Birkeland, 1979; Smirnova and Nikonov, 1990; Ren and Li, 1993; Noller and Locke, 2000; Ehlmann et al., 2008). These methods are simple and inexpensive. However,

* Corresponding author. Tel.: +86 10 62009215.
E-mail addresses: weizhanyu@gmail.com (Z. Wei), honglinhe123@vip.sina.com, honglin@ies.ac.cn (H. He), skywazy@126.com (F. shi).

0191-8141/$ – see front matter © 2013 Elsevier Ltd. All rights reserved.
http://dx.doi.org/10.1016/j.jsg.2013.08.008

because it is labor intensive, only a few samples were reported for each surface, and the results are vulnerable to the operators' experience and subjectivity. Progressive surface weathering often leads to increased surface roughness; the more eroded by weathering the topography is, the rougher the surface. Surface roughness could be an indicator of the degree of weathering of the rock surface (McCarroll and Nesje, 1996).

The aim of this research is to quantify the degree of weathering of a bedrock fault surface, which is meaningful in building a relationship between exposure time and degree of weathering. We chose a limestone fault surface near Beijing and measured its topography utilizing ground-based LiDAR (Light Detection And Ranging), which is popular for measuring the topography of fault surfaces in the field (Sagy et al., 2007; Brodsky et al., 2010; Wei et al., 2010). After reviewing the methodology, we presented roughness measurements in the form of power spectral density in directions parallel and perpendicular to the slip. A new approach for quantifying the progressive degree of weathering of a bedrock fault surface based on surface roughness is proposed, and the result shows that the roughness in a high frequency band depends on the exposure time of the fault surface. Finally, we discuss how this new approach could be used to evaluate the exposure time or even the faulting time of a bedrock fault surface.

2. Scanned fault scarp and its geologic site

Nearly adjacent to the Tibetan Plateau, the Ordos block bridges the intensively uplifted Plateau and the disassembled old North China Craton (Jolivet et al., 2001; Wang et al., 2011). Surrounding the block, four faulted-depression basin belts develop: Shanxi Faulted-depression Basin Belt (SFB) in east, Yinchuan-Jilantai Faulted-depression Basin Belt (YFB) in west, Hetao Faulted-depression Basin Belt (HFB) in north and Weihe Faulted-depression Basin Belt (WFB) in south (Xu and Ma, 1992; Deng et al., 1999) (Fig. 1a). In these faulted-depression basins, a lot of fault scarps crop out.

The Shizhuang fault, our target fault is an active fault in Late Pleistocenc-Holocene era (Ran et al., 1992), and crosses the Yanhuai basin in the direction of 300°–320° and dips northeastward at 60°–80° (Fig. 1b). The Huailai basin located northwest of Beijing, is one of the faulted-depression basins in the Shanxi Faulted-depression Basin Belt (Fig. 1a). The scanned fault scarp crops out

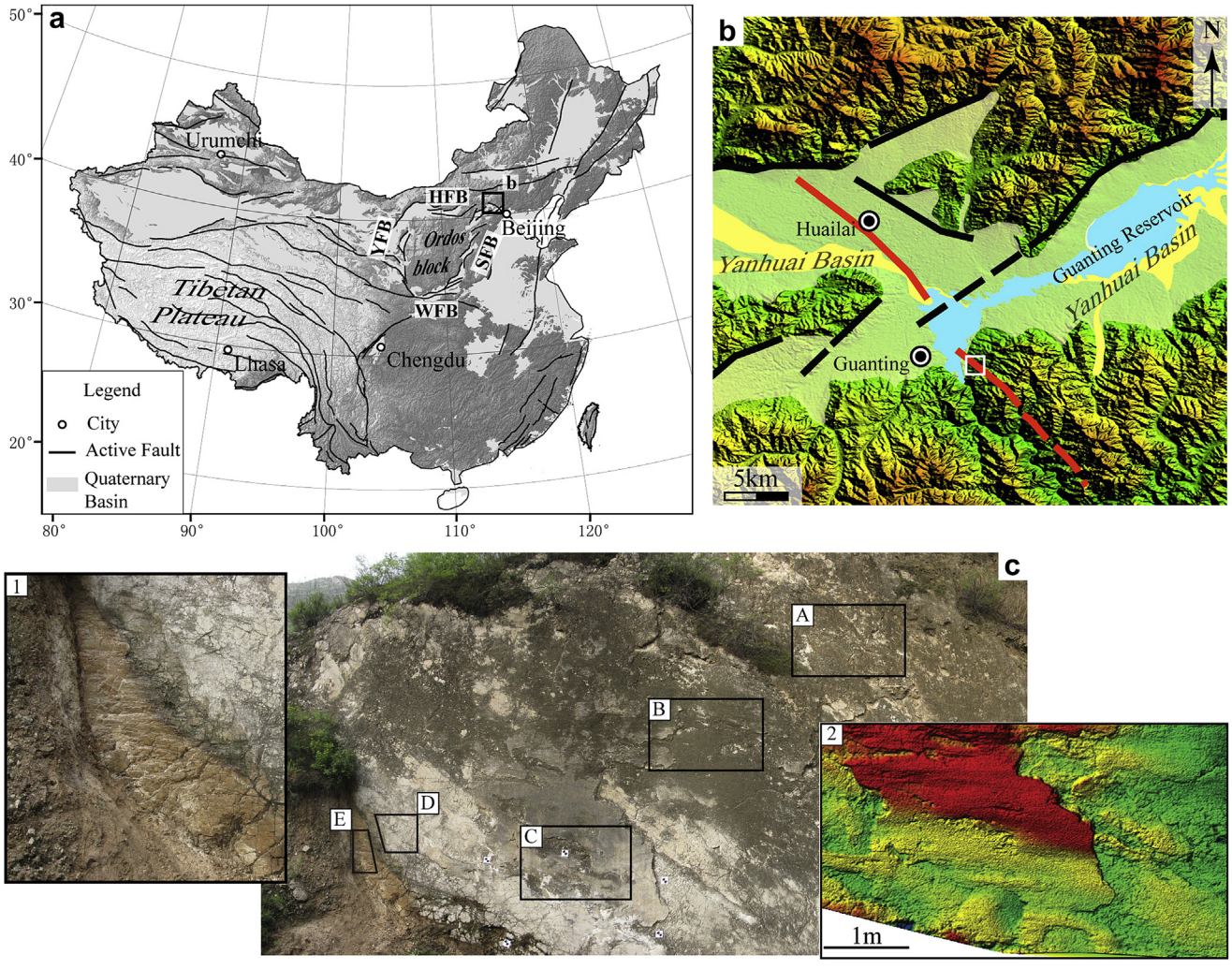

Fig. 1. Sketch map on tectonics of China and fault surface pictures. (a) Main active fault distribution of China (modified from Deng, 2007), black lines indicate active faults; black rectangle shows the location of (b); (b) Topographical map and fault distribution in Yanhuai Basin. Red lines indicate Shizhuang Fault and black lines indicate other faults; the base map is from ASTER Global DEM data; white rectangle shows the location of (c); (c) Photographs of the target fault surface. Five black boxes, labeled A, B, C, D and E, show the locations of the scanned surface patches. Inset 1 is the enlarged view of excavated patch E; Inset 2 is the LiDAR image of the target fault surface in color-scale produced by – one million scanning points with 5-mm-spacing on average. (For interpretation of the references to color in this figure legend, the reader is referred to the web version of this article.)

in a small valley near Shizhuang village in northwest Beijing, China (Fig. 1b). It is produced by strike-slip faulting on the Shizhuang fault. The bedrock on either side of the fault is different. The sediments outcropping in the northeastern fault wall are well stratified Pliocene conglomerate with pebbles and red clay matrix; the stratum in the other wall is dolomite of the middle Proterozoic era. The fault surface presents a dolomite fault scarp on the southwestern wall.

The fault surface is an area 10 m high and 50 m wide on the dolomite fault scarp (Fig. 1c). Large elongated bumps and depressions associated with striations on the surface are visible, plunging northwest 5°, indicating major strike-slip faulting with a minor normal faulting component.

The topography of the fault surface is not uniform. Based on the degree of weathering, it can be zoned into different height units that are related to the duration of exposure to weathering. The higher the surface is, the longer the weathering process and the more serious the erosion. Furthermore, the more deeply weathered surface is usually colonized by lichen. Despite weathering and lichen colonizing, the mechanical striations induced by faulting can be still recognized on the surface. The lower part of the surface is relatively clean due to slight weathering and no lichen colonization, and the striations are more easily recognizable. To examine the mantle effect of weathering, we excavate a surface patch of 1 m × 0.5 m covered by unconsolidated sediment on the bottom of the surface (patch E in Fig. 1c).

3. Data collection and analysis method

3.1. Data acquisition

We chose five typical surface patches based on different weathering characteristics in the target fault surface of approximately 55 m^2 (Fig. 1c). Patch A is located at the upper part of the fault surface and has deeper weathering because of longer exposure; patch B is located at the middle and has moderate weathering; patches C and D are located at the lower part and have slight weathering. patch E is the excavated surface on the bottom of the surface. The topography of the fault surface was determined using a three-dimensional LiDAR Scanner, and these chosen patches were measured accurately, with adjacent points spaced no greater than 2 mm apart. The LiDAR scanner (Trimble GX) used here can precisely measure distance over hundreds of square meters with point spacing as close as 1 mm. The topographic fault surface data collected by the LiDAR scanner are sets of point clouds. All non-fault features (e.g., trees, grass) can be removed in post-processing of the point clouds.

Once all non-fault features are removed, the scanning data are then rotated so that the fault strike-line and the dipping line are the *X*-axis and *Y*-axis, respectively, and the fluctuation direction of the fault surface is the *Z*-axis. These data sets of 3D point clouds are transformed into 2 + 1D data sets corresponding to Digital Elevation Models (DEMs) (Fig. 2), which are the basis for characterizing the amplitude of the roughness at various spatial wavelengths. When considering the natural fault surface, local weathering pits and/or the presence of vegetation may form small patches of

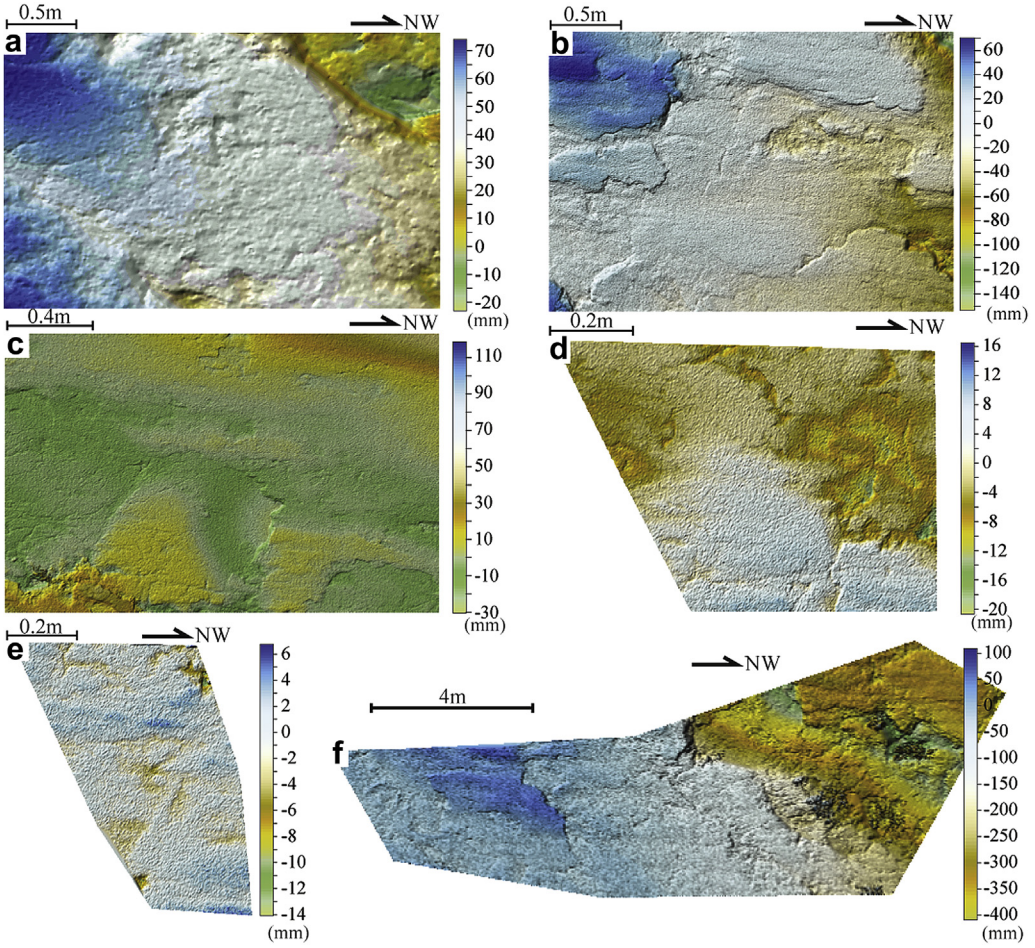

Fig. 2. Digital Elevation Models (DEMs) as color-scale maps of different scanning patches on fault surface with adjacent points spaced no greater than 2 mm (a), (b), (c), (d) and (e) correspond to those areas indicated by rectangles in Fig. 1. (f) LiDAR image of whole fault surface with 5-mm-spacing between adjacent points.

missing data, which are less than 3% of the total data. We fill the missing data gap using natural Neighbor interpolation. Candela et al. (2009) have proven that interpolation of missing data does not significantly affect the measurement of surface topographic properties, regardless of the analysis technique employed.

3.2. Methods

Like many other natural surfaces, roughness is the most obvious characteristic of the natural fault surface. To quantify fault roughness, we calculate the values of the power spectral densities of profiles in directions parallel and perpendicular to the slip (Power et al., 1987, 1988; Brown, 1995; Sagy et al., 2007, 2009). Power spectral density is a mathematical method based on time series analysis performing a Fourier decomposition to convert data from the space domain to the frequency domain. The contribution of different wavelengths to the roughness of a fault surface can be found by measuring the strength of the sinusoidal component. This is a reliable method to calculate roughness when it is based on many profiles (Simonsen et al., 1998; Candela et al., 2009), and has been widely used to describe the natural fault surface. Power and Tullis (1991) and Perron et al. (2008) introduced the calculation steps and processing details of spectral analysis, such as the Nyquist cutoff, spectral leakage and window functions. Candela et al. (2009) gave a detailed discussion on the systemic error of spectral analysis.

Self-similar and self-affine models are compared to the surface data ranging from natural fractures and joints (Brown and Scholz, 1985) to natural fault surfaces (Power et al., 1988, 1991; Sagy et al., 2007, 2009), even to surface earthquake ruptures (Candela et al., 2012) over a large range of scales. Over a restricted range of wavelengths, topographic data in spectral space can be fit by a power law of the form:

$$G(f) = Cf^{-\alpha} \quad (1)$$

where G(f) is power spectral density and f is spatial frequency. Least squares regression of log [G(f)] versus log (f) determines the slope ($-\alpha$) and intercept log (C) of the power spectral (Fig. 3). $-\alpha$

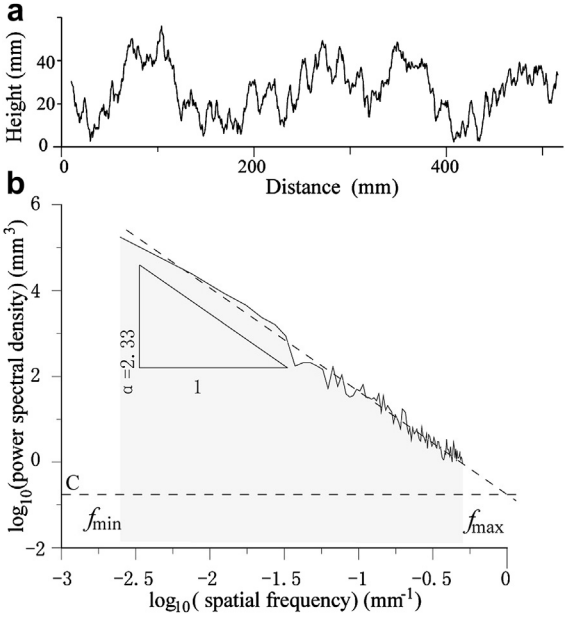

Fig. 3. 1-D profile generated using an algorithm method (a) and the description of power spectral density (b). (a) Representative 1-D profile extract in a 2D synthetic self-affine fault surface by an algorithm method (Candela et al., 2009). (b) Power spectral density is described by a regression line with slope $-\alpha$ and intercept log (C).

determines how the surface topography changes or 'scales' with wavelength (Power and Tullis, 1991; Lee and Bruhn, 1996), ranging between −3 and −2 for the fault surface. On a natural fault surface, the slope ($-\alpha$) of the power spectral density curve is not consistent but varies in different frequency bands, showing scale-dependent characteristics. For simplicity, one surface is rougher than another at a given wavelength if its power spectral density is higher. This function is usually used to interpret the relative roughness of a suite of fault surfaces.

Generally, slope and characteristic length are the two parameters used to characterize the topography of a fault surface. The characteristic length is the wavelength corresponding to the inflections of slope that separates the neighboring two bands with different segment slopes (Ohnaka and Shen, 1999). However, various explanations for the scale-dependent characteristics of surface topography have been suggested by laboratory experiments (Chen and Spetzler, 1993; Ohnaka, 2003) and field measurements (Scholz and Avites, 1986; Power et al., 1987; Brown and Scholz, 1985). It is widely recognized that the scale of characteristics and characteristic length play an important role in rupture nucleation (Ohnaka and Shen, 1999; Scholz, 2002), the mechanics of fault slip (Power et al., 1987). As will be demonstrated later, the characteristic length is also related to the weathering topography for fault outcrops.

4. Results

We calculated the power spectral density of each fault patch in directions parallel and perpendicular to the slip. Each spectral curve represents an average over a large set of 1-D profiles that are extracted from the DEM of each fault patch and parallel to each other. In general, the power spectral density and spatial frequency typically follow a power law for each fault patch, showing approximately linear relationships with slopes between −2 and −3 in the log–log plot (Fig. 4). Spectrum A corresponds to the more deeply weathered surface on which the polished surface material has been removed, leaving gray pitting; Spectral B comes from the moderately weathered patch; Spectral C and D correspond to the smooth and slightly weathered patches. Spectral E corresponds to the excavated fault surface without exposure to weathering. The spectral densities within different patches indicate an obvious discrepancy of roughness. The rougher the patch is, the higher the spectral density is; patch A is the roughest, and patch E is the smoothest.

For all patches, power spectral densities in the direction perpendicular to the slip are larger than those in the direction parallel to the slip (Fig. 5), showing that profiles perpendicular to the slip generally have more power than those parallel to the slip. This means that the direction perpendicular to the slip is always rougher than the direction parallel to the slip. Moreover, all spectral curves, either perpendicular or parallel to the slip, can be divided into two segments based on careful visual inspection. In the lower frequency band, the spectral curve is close to the fitting line; in the higher frequency band, the spectral curve deviates from the fitting line, forming an upward bulge (Fig. 5). In the direction parallel to the slip, the power curve rises and approaches those perpendicular to the slip in the higher frequency band. We ascribe this variation to natural weathering of the exposed fault surface within the higher frequency band.

5. Discussion

5.1. Scaling property of surface roughness

The topography of the fault surface is an interacting product of wear in the faulting process and erosion in the weathering process. Although fault surfaces generally emerge from the ground as smooth, polished planes, high-resolution studies both in the laboratory and

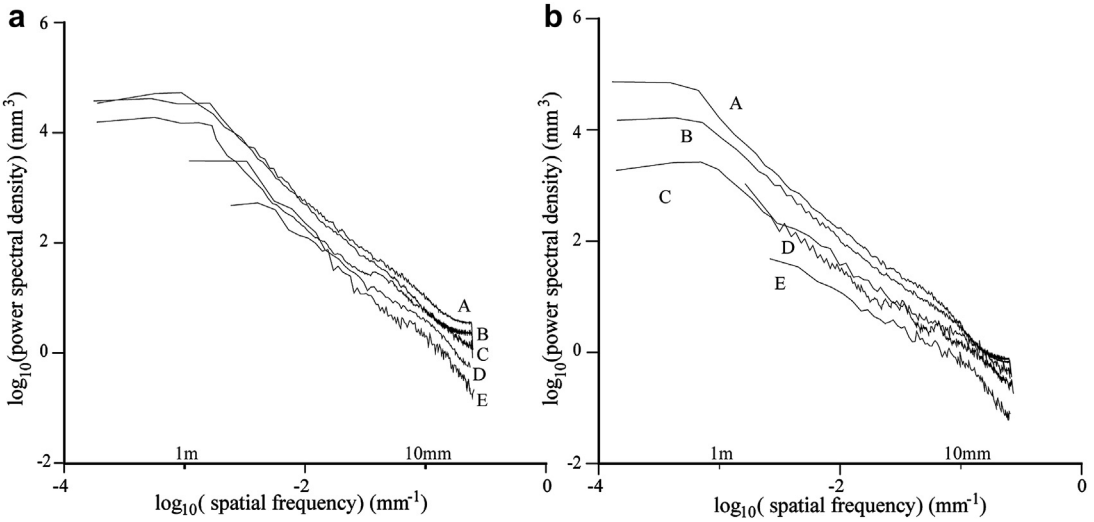

Fig. 4. Power spectral for five surface patches labeled A, B, C, D and E in Fig. 2. Power spectral densities are calculated from profiles measured perpendicular to the slip (a) and parallel to slip (b).

the field have shown that at the outcrop scale, fault surfaces possess an inherent roughness which can, in turn, be accentuated by weathering (Brown and Scholz, 1985; Power et al., 1987, 1988). Previous studies of natural fault roughness measured by power spectral density suggested a change in scaling properties between large and short length scales, and a different slope can be calculated for each band (Power and Tullis, 1991; Chen and Spetzler, 1993; Lee and Bruhn, 1996). However, due to technical limitations, previous measurements of the fault surface were not sufficiently accurate to decipher what this variation was related to, surface weathering or the faulting process (Candela et al., 2009). Power et al. (1987) suggested that later degradation of the natural fault surface by weathering could introduce more power in their spectral values, which might influence the change of slope. Based on laboratory experiments, Chen and Spetzler

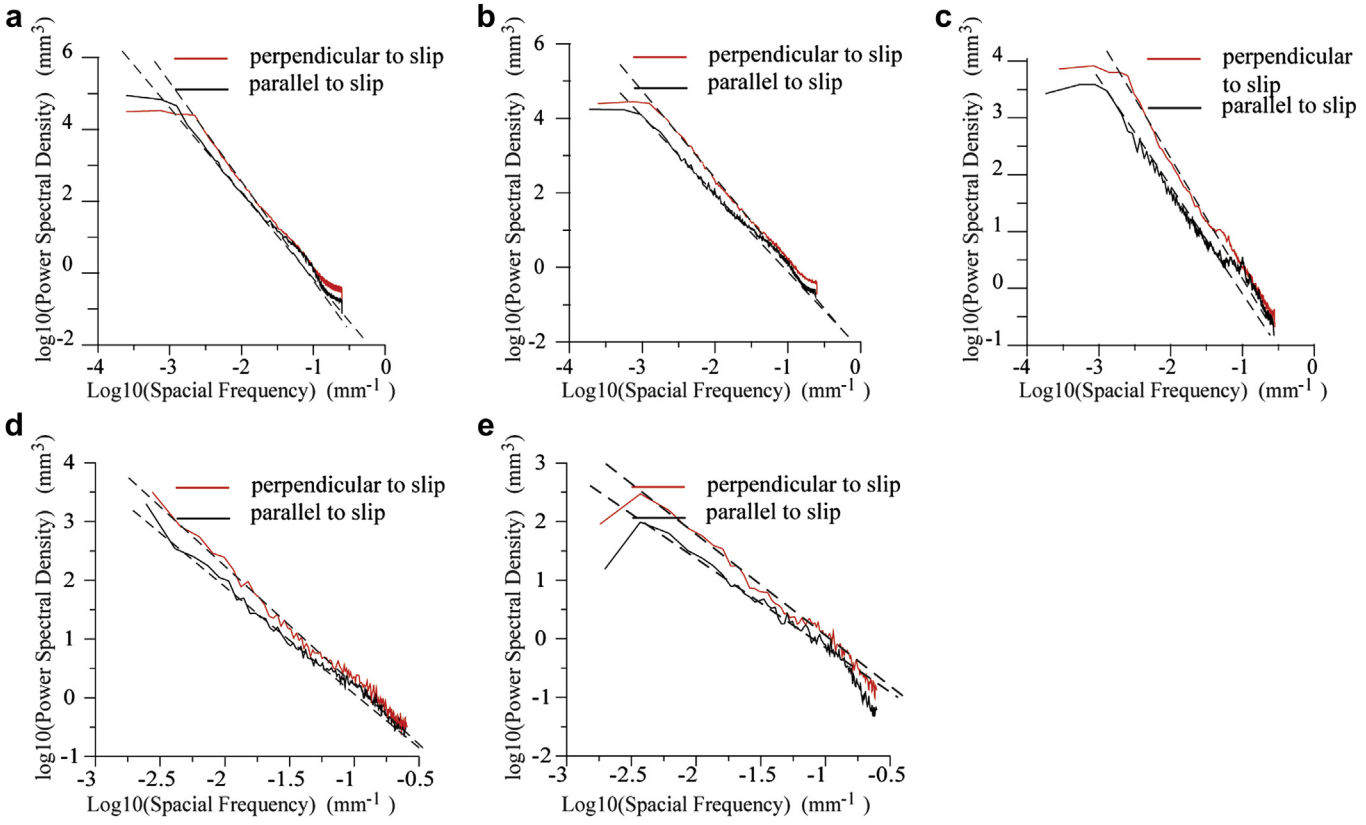

Fig. 5. Power spectral density in directions perpendicular (red) and parallel (black) to slip. The dashed line is the least squares fitting line of spectral curves perpendicular to and parallel to slip. a, b, c, d and e correspond to patches A, B, C, D and E. (For interpretation of the references to color in this figure legend, the reader is referred to the web version of this article.)

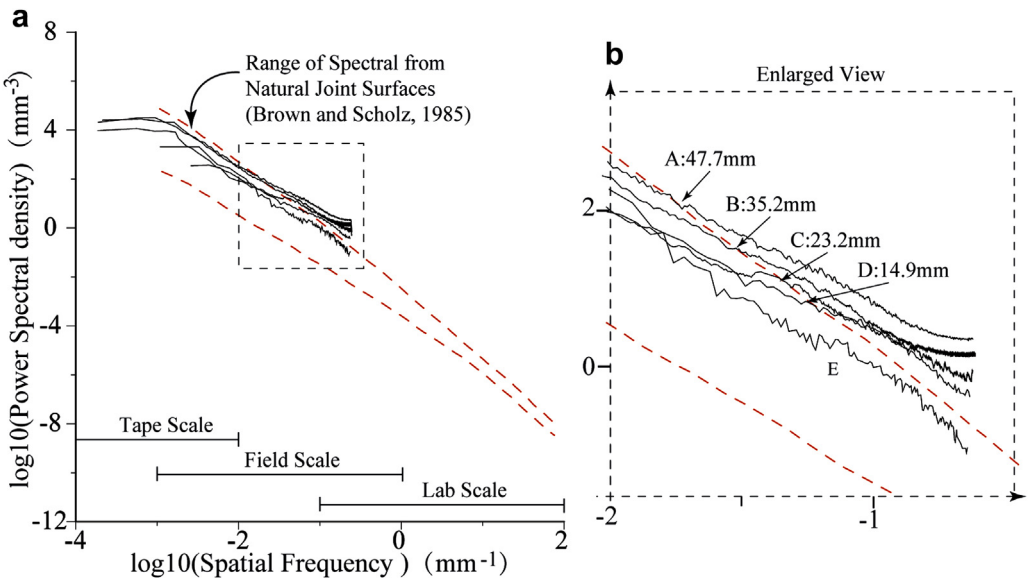

Fig. 6. Power spectral density in the direction perpendicular to slip. Two dashed red lines enclose the area where power spectral values from natural joint surfaces would fall (Brown and Scholz, 1985). (a) Due to weathering erosion, all power spectral values except for that of patch E depart from the area outlined by the dashed red line in the higher frequency band. (b) Enlarged view of the high frequency section delineated by the black box in (a), spectral curves of different fault patches with different degrees of weathering have different wavelengths corresponding to the offset points. (For interpretation of the references to color in this figure legend, the reader is referred to the web version of this article.)

(1993) suggested that the break slope at length scales of several millimeters was caused by a change in the dominant mode of deformation from small-scale to large scale intragranular cracking. In our study, we have also observed changes of the power spectral slope between different wavelength bands, and this is particularly clear for spectral curves parallel to the slip (Fig. 5).

In a large scale of several meters to kilometers, fault topography and geometric irregularity may reflect the process of lateral growth and linking together of several fault surfaces during the early evolution of the fault zone (Lee and Bruhn, 1996; Lohr et al., 2008). The slip distance during one faulting event is typically several meters or less, and considerable wear must take place during faulting (Scholz, 2002). This results in the fact that the fault surfaces in the direction parallel to the slip are smoother than the natural joint surface (Brown and Scholz, 1985); therefore, the topography of the fault surface at this scale (several centimeters – several meters) is dominated by faulting activity. Once the fault surface is exposed, weathering rebuilds the topography of the fault surface in the small scale. Erosion generates pitting several millimeters to several centimeters in size and roughens the surface that was once smooth when it emerged from the ground. The topography of the fault surface in the small scale is controlled by weathering, and the weathered topography should provide a measure of exposure time. Therefore, the topographic features at different spatial scales are related to different mechanical processes.

5.2. Quantify the weathering of the fault surface

For a bedrock fault surface exposed in past faulting events, the analysis of weathering features may represent a tool for defining a succession of faulting events (Stewart, 1996; Giaccio et al., 2002). Here, we introduce a new approach to quantify the weathering degree of a fault surface according to roughness in the form of power spectral density.

5.2.1. Deviation from normal spectral range

The topography of the fault surfaces in the direction perpendicular to the slip have a comparable roughness to a natural joint surface without shear wear; along the slip, however, mechanical wear processes reduce the amplitude of the roughness (Power et al., 1987; Sagy and Brodsky, 2009). Brown and Scholz (1985) calculated the range of the power spectral values of various natural joint surfaces (the area outlined by the dashed red lines in Fig. 6) under every scale. On a natural fault surface, the power spectral value in the direction perpendicular to the slip would fall into this area, showing that the roughness of a natural fault surface in the direction perpendicular to the slip is similar to that of a natural joint surface (Power et al., 1987, 1991). Our analysis of roughness is similar to that of previous studies: the power spectral value in the direction perpendicular to the slip falls into the spectral range calculated by Brown and Scholz (1985) (Fig. 6). In the high frequency band, however, all spectral curves deviate upward from the spectral range except patch E without exposure to weathering. The wavelengths corresponding to the offset points of surface patches A, B, C and D are different from each other. patch A (the uppermost section), with deeper weathering, has the longest offset wavelength of 47.7 mm, and patch D, with slight weathering, has the shortest offset wavelength of 14.9 mm patches B and C have wavelengths corresponding to offset points 35.2 mm and 23.2 mm, respectively. We can find a simple relationship between weathering and the wavelength of the offset point. The greater the weathering of the fault surface, the longer the wavelength corresponding to the offset point is.

5.2.2. Inflection from the fitting line

As mentioned above, the power spectral curve, either perpendicular or parallel to the slip, is close to the fitting line in the lower-frequency band but deviates from the fitting line in the higher frequency band and forms an upward bulge due to exposure to weathering. Therefore, the wavelength of the inflection point from the fitting line can also be used to quantify the exposure to weathering of a fault surface similar to the deviation from the normal spectral range. To obtain the wavelength of the inflection point, we calculated the curvature (the second derivative) of the spectral curve and plotted it to frequency (Figs. 7 and 8, right). The frequency corresponding to the inflection point was identified as

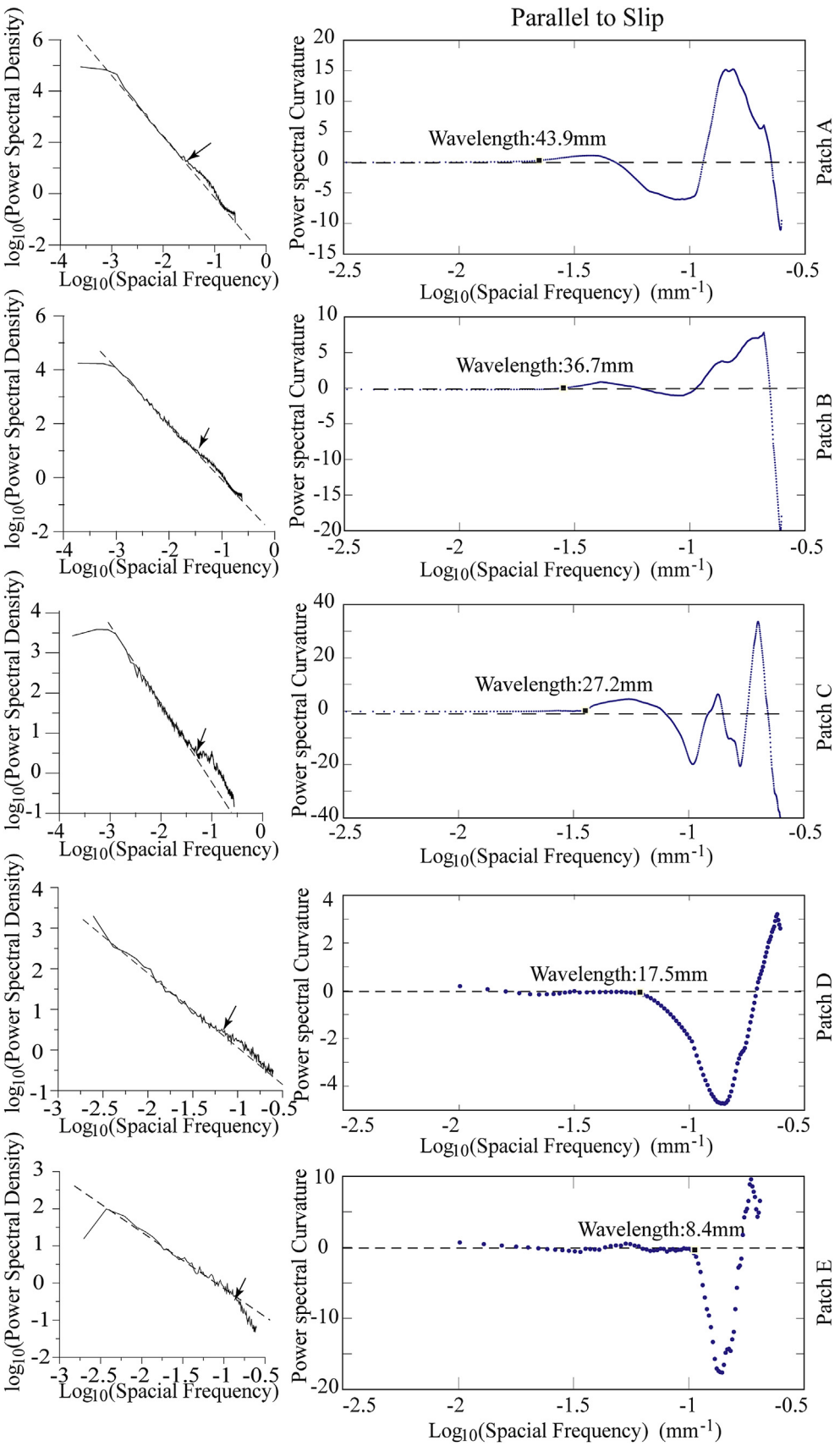

Fig. 7. Power spectral density (left) and the curvature calculated from power spectral values (right) in the directions parallel to slip. At left, the real curves are power spectral densities and dashed lines indicate the attenuation trend of power with increasing frequency by least-square fitting; at right, the dotted curves are the curvatures of power spectral curves. Arrows (left) and round dots (right) indicate the locations corresponding to inflection points identified as the points at which the curvatures begin to wave.

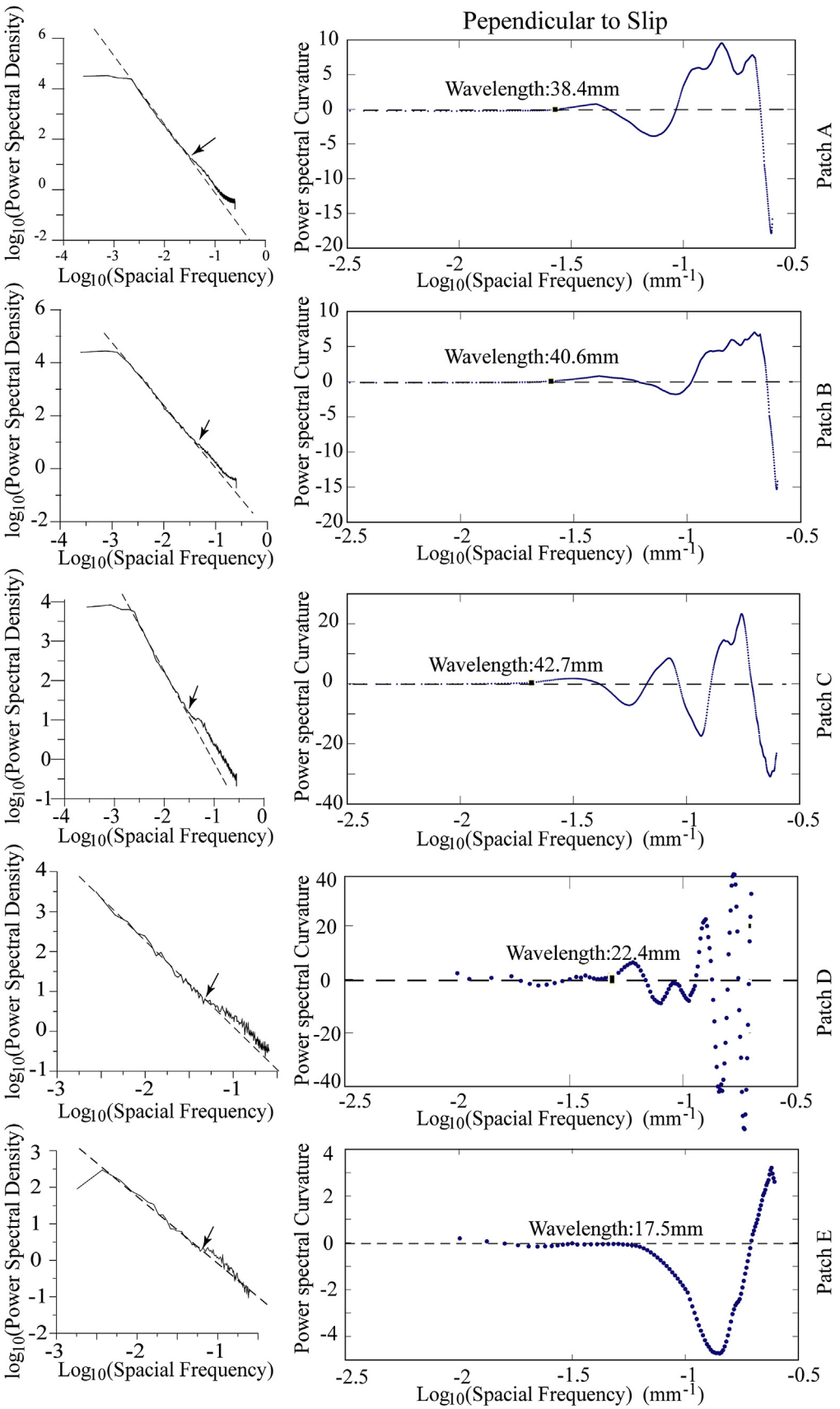

Fig. 8. Power spectral density (left) and the curvature calculated from power spectral values (right) in the directions perpendicular to slip. At left, the real curves are power spectral densities and dashed lines indicate the attenuation trend of power with increasing frequency by least-square fitting; at left, the dotted curves are the curvatures of power spectral curves. Arrows (left) and round dots (right) indicate the locations corresponding to inflection points identified as the points at which the curvatures begin to wave.

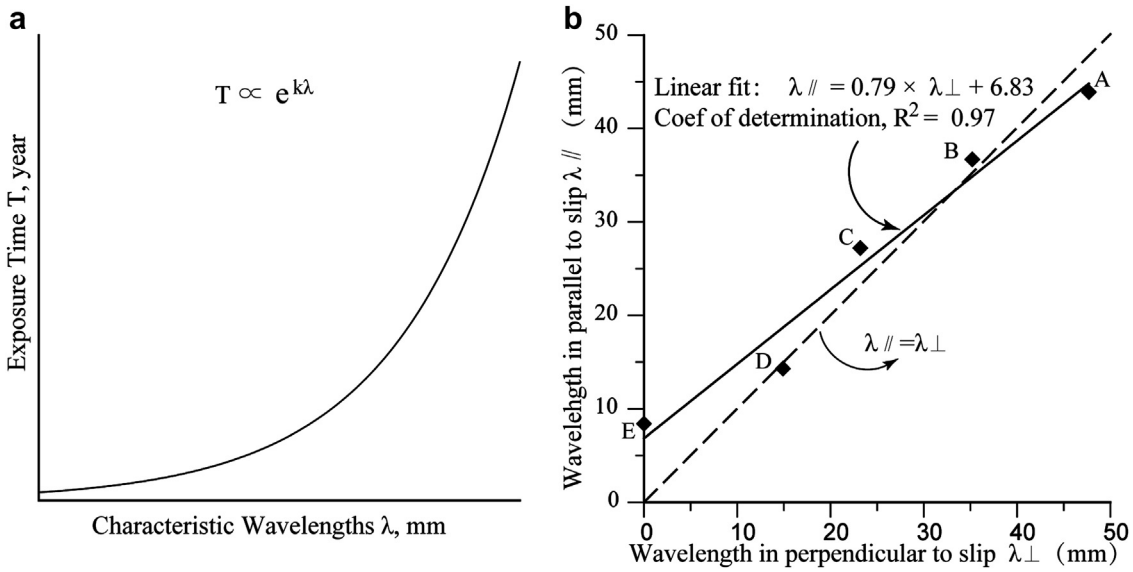

Fig. 9. (a) Schematic diagram of the exponential relationship between the characteristic wavelengths and exposure time. (b) Illustration of the relationship between characteristic wavelengths corresponding to deviation points in the direction perpendicular to slip and corresponding to inflection points in the direction parallel to slip. The straight solid line is the least squares fitting line, $\lambda_{//} = 0.79 \times \lambda_{\perp} + 6.83$; the dashed line is function $\lambda_{//} = \lambda_{\perp}$.

the point at which the curvature begins to wave. This procedure yielded wavelengths corresponding to the inflection points for all surface patches, either perpendicular or parallel to the slip.

In the direction parallel to the slip, the wavelength corresponding to the inflection point of surface patch A with the deepest weathering is 43.9 mm, and the wavelengths for patches B, C, D and E gradually decrease as weathering weakens, 36.7 mm, 27.2 mm, 14.3 mm and 8.4 mm, respectively (Fig. 7 right). Although patch E is covered by unconsolidated sediment without exposure to weathering, the emergence of the inflection point of 8.4 mm indicated that some weathering might have occurred under the unconsolidated sediment. Therefore, we speculate that the greater the weathering of the fault surface is, the longer the wavelength corresponding to the inflection point. As the weathering increases, the inflection point moves toward the lower frequency.

In the direction perpendicular to the slip, the wavelengths corresponding to the inflection points of surface patches A, B, C, D and E are 38.4 mm, 40.6 mm, 42.7 mm, 22.4 mm and 17.5 mm, respectively (Fig. 8). The wavelength corresponding to the inflection point has no linear relationship with the exposure to weathering of the fault surface, neither proportional to nor inversely proportional to exposure to weathering, but inclines to a predominant wavelength of approximately 40 mm as the weathering deepens. Therefore, the wavelength corresponding to the inflection point identified in the direction perpendicular to the slip is not a useful parameter to describe the weathering of a fault surface.

The weathering effect on surface topography is not identical in directions parallel and perpendicular to the slip, and it seems that roughness in the direction parallel to the slip is more sensitive to weathering than that in the direction perpendicular to the slip. Candela et al. (2009) have also confirmed the discrepancy between different directions. They simulate the effect of weathering by adding a noise signal in the rough signal, and experimental results proved that weathering has a stronger effect on the profiles parallel to the slip because they are characterized by a smaller amplitude compared to the profiles perpendicular to the slip. The mechanical wear caused by faulting makes the fault surface smooth in the direction parallel to the slip more than in the direction perpendicular to the slip. Furthermore, striations and grooves approximately 5 mm–20 mm wide on the fault surface have been observed in the field. The profiles perpendicular to the slip have salient sinusoidal fluctuations with wavelengths of 10 mm–40 mm, twice the striations' width. More smoothness makes the roughness in the direction parallel to the slip more sensitive to weathering than that in the direction perpendicular to the slip, while the lower characteristic frequency caused by faulting makes rebuilding the topography of the fault surface in the direction perpendicular to the slip by weathering occurring at a higher frequency more difficult than that in the direction parallel to the slip. Therefore, only the wavelength corresponding to the inflection point in the direction parallel to the slip was chosen here to quantify the weathering of the fault surface.

The surface patches A – D located at different heights have different wavelengths corresponding to both deviation points perpendicular to the slip and inflection points parallel to the slip. These wavelengths can be used to quantify the degree of weathering of a fault surface. If the result is calibrated, it is possible to build a relationship between the degree of weathering and the exposure time of the fault surface. Such a relationship would be useful to identify paleoearthquakes where a bedrock fault scarp exists, similar to the application of morphologic dating to colluvial and alluvial scarps.

5.3. *Degree of weathering as a function of exposure time of the fault surface*

As discussed above, two types of wavelengths ($\lambda_{//}$ and $\lambda_{\perp}$) had been used to quantify weathering of the bedrock fault surface based on different methods perpendicular and parallel to the slip. Many methods have been developed to estimate the age of rock exposure based on the time-dependent topographic model of the rock surface as weathering, and other weathering phenomena such as weather pits, etching and roughness have been used as a function of exposure time (Colman and Pierce, 1986). In a similar way, we assumed characteristic wavelengths corresponding to deviation points or inflection points to be an exponential function of exposure time (Equations (2) and (3); Fig. 9a). Thus, Thus, in directions parallel and perpendicular to the slip, the functions are the following:

$$T = c_{//} e^{k_{//}\lambda_{//}} \quad (2)$$

$$T = c_{\perp} e^{k_{\perp}\lambda_{\perp}} \quad (3)$$

where c and k are constants, T is exposure time and λ is wavelength. Combining Equations (2) and (3), we obtain a function of the characteristic wavelengths corresponding to deviation points or inflection points as follows, which indicates a linear correlation between $\lambda_{//}$ and $\lambda_{\perp}$.

$$\lambda_{//} = \frac{k_{\perp}}{k_{//}}\lambda_{\perp} + \frac{\left(\ln(c_{\perp}) - \ln\left(c_{//}\right)\right)}{k_{//}} \quad (4)$$

Plotting the characteristic wavelengths corresponding to deviation points or inflection points ($\lambda_{\perp}$ and $\lambda_{//}$) and linear fitting, we obtained the following relationship: $\lambda_{//} = 0.79 \times \lambda_{\perp} + 6.83$ (Fig. 9b). This relationship confirms that Equation (3) indeed exists and supports our new approaches to quantifying the weathering of the fault surface reasonably and applicably.

6. Conclusions

The morphologic analysis of the Shizhuang fault scarp proves that bedrock fault topography may indeed exhibit time-dependent morphological changes related to scarp degradation; the longer the exposure time is, the rougher the surface is. Because higher areas correspond to longer weathering history, higher fault surfaces exhibit more roughness than lower surfaces. Moreover, our analysis shows that different processes control the topography of the fault surface at different spatial scales. The frictional wear during faulting and ploughing of asperities predominantly controls the surface texture at a scale of a few meters or more, while weathering predominantly controls the surface texture at the scale of a few centimeters or less.

Later degradation of the natural fault surface by weathering could introduce additional power in power spectral values. The deeper the weathering is, the more power is introduced. By comparing roughness in the form of power spectral density, weathering of the fault surface can be quantified by two wavelengths: wavelengths ($\lambda_{\perp}$) in which spectral curves deviate upward from the spectral range in a direction perpendicular to the slip, and wavelengths ($\lambda_{//}$) corresponding to the inflection point of curves in a direction parallel to the slip. These two types of wavelengths are positively correlated with the degree of weathering.

Although there is an obvious linear relationship between the two types of characteristic wavelengths ($\lambda_{//} = 0.79 \times \lambda_{\perp} + 6.83$), which complies with the hypothesis that characteristic wavelengths are an exponential function of exposure time, it is necessary to calibrate the absolute exposure time of the fault surface using a useful dating technique, such as the cosmogenic nuclides dating method, before the weathering topography of the bedrock fault surface can become a valuable tool to reconstruct paleoseismic history.

Acknowledgments

The authors would like to thank Prof. Yongkang Ran for great assistance in the field and for discussions about the weathered bands along bedrock fault scarps. Special thanks to George Hilley and to Biagio Giaccio for helpful suggestions and comments that substantially improved this paper. This research was supported by the National Natural Science Foundation of China (grant number: 40872128) and Basic Research Fund from Institute of Geology, China Earthquake Administration (grant number: IGCEA1113).

References

Andrews, D.J., Hanks, T.C., 1985. Scarp degraded by linear diffusion: inverse solution for age. J. Geophys. Res. 90, 10193–10208.
Arrowsmith, J.R., Rhodes, D.D., Pollard, D.D., 1998. Morphologic dating of scarps formed by repeated slip events along the San Andreas Fault, Carrizo Plain, California. J. Geophys. Res. 103, 10141–10160.
Benedetti, L., Finkel, R., Armijo, R., Papanastasiou, D., Ryerson, F.J., King, G.C., Flerit, F., Farber, D., Caffee, M., 2000. Earthquake time-slip histories determined from in situ ^{36}Cl cosmogenicdating of limestone fault scarps: the Normal Fault (Greece). Eos, Trans., AGU 81 (48). Fall Meeting, Abstract T71E-10.
Birkeland, P.W., Noller, J.S., 2000. In: Noller, J.S., Sowers, J.M., Lettis, W.R. (Eds.), Rock and Mineral Weathering, Quaternary Geochronology: Methods and Applications, vol. 4, pp. 293–312 (Washington, D. C).
Brodsky, E.E., Gilchrist, J.J., Sagy, A., Collettini, C., 2010. Fault smooth gradually as a function of slip. Earth. Planet. Sci. Lett. 302, 185–193.
Brown, S.R., Scholz, C.H., 1985. Broad bandwidth study of the topography of natural rock surfaces. J. Geophys. Res. 90, 2575–2582.
Brown, S.R., 1995. Simple mathematical model of a rough fracture. J. Geophys. Res. 100, 5941–5952, http://dx.doi.org/10.1029/94JB03262.
Burke, R.M., Birkeland, P.W., 1979. Reevaluation of multiparameter relative dating techniques and their application to the glacial sequence along the eastern escarpment of the Sierra Nevada, California. Quaternary Res. 11, 21–51.
Candela, T., Renard, F., Bouchon, M., Marsan, D., Schmittbuhl, J., Voisin, C., 2009. Characterization of fault roughness at various Scales: implications of three-dimensional high resolution topography measurements. Pure Appl. Geophys. 166, 1817–1851.
Candela, T., Renard, F., Klinger, Y., Mair, K., Schmittbuhl, J., Brodsky, E.E., 2012. Roughness of fault surfaces over nine decades of length scales. J. Geophys. Res. 117, B08409. http://dx.doi.org/10.1029/2011JB009041.
Chen, G., Spetzler, H.A., 1993. Topographic characteristics of laboratory-induced shear fractures. Pure Appl. Geophys. 40, 123–135.
Colman, S.M., Pierce, K.L., 1986. The glacial sequence near McCall, Idaho: weathering rinds, soil development, morphology and other relative-age criteria. Quaternary Res. 25, 25–42.
Deng, Q.D., Cheng, S.P., Min, W., et al., 1999. Discussion on cenozoic tectonics and dynamics of Ordos block. J. Geomech. 5 (3), 13–21.
Deng, Q.D., 2007. Active Tectonic Map of China (in Chinese). Earthquake Publishing House.
Ehlmann, B.L., Viles, H.A., Bourke, M.C., 2008. Quantitative morphologic analysis of boulder shape and surface texture to infer environmental history: a case study of rock breakdown at the Ephrata Fan, Channeled Scabland, Washington. J. Geophys. Res. 113, F02012. http://dx.doi.org/10.1029/2007JF000872.
Giaccio, B., Galadini, F., Sposato, A., Messina, P., Moro, M., Zreda, M., Cittadini, A., Salvi, S., Todero, A., 2002. Image processing and roughness analysis of exposed bedrock fault planes as a tool for paleoseismological analysis: results from the Campo Felice fault (central Apennines, Italy). Geomorphology 49, 281–301.
Jolivet, M., Brunel, M., Sevard, D., et al., 2001. Mesozoic and cenozoic tectonics of the northern edge of the Tibetan Plateau: fission track constrains. Tectonophysics 343, 111–134.
Lee, J.J., Bruhn, R.L., 1996. Structural anisotropy of normal fault surfaces. J. Struct. Geol. 18, 1043–1059. http://dx.doi.org/10.1016/0191-8141(96)00022-3.
Lohr, T., Krawczyk, C., Oncken, O., Tanner, D., 2008. Evolution of a fault surface from 3D attribute analysis and displacement measurements. J. Struct. Geol. 30 (6), 690–700.
Mayer, L., 1984. Dating Quaternary fault scarps formed in alluvium using morphologic parameters. Quaternary Res. 22, 300–313.
McCarroll, D., Nesje, A., 1996. Rock surface roughness as an indicator of degree of rock surface weathering. Earth Surf. Proc. Land. 21 (10), 963–977.
Mitchell, S.G., Matmon, A., Bierman, P.R., Enzel, Y., Caffee, M., Rizzo, D., 2001. Displacement history of a limestone normal fault scarp, northern Israel, from cosmogenic ^{36}Cl. J. Geophys. Res. 106, 4247–4264.
Nash, D.B., 1986. Morphologic dating and modelling degradation of fault scarps. In: Wallace, R.E. (Ed.), Active Tectonics, Studies in Geophysics. National Academy Press, Washington, DC, pp. 181–194.
Noller, J.S., Locke, W.W., 2000. In: Noller, J.S., Sowers, J.M., Lettis, W.R. (Eds.), Lichenometry, Quaternary Geochronology: Methods and Applications, vol. 4, pp. 261–272. Washington, D. C.
Ohnaka, M., Shen, L.F., 1999. Scaling of the shear rupture process from nucleation to dynamic propagation: implications of geometric irregularity of the rupturing surface. J. Geophys. Res. 104, 817–844.
Ohnaka, M., 2003. A constitutive scaling law and a unify comprehension for frictional slip failure, shear fracture of intact rock, and earthquake rupture. J. Geophys. Res. 108 (B2), 2080. http://dx.doi.org/10.1029/2000JB000123.
Perron, J.T., Kirchner, J.W., Dietrich, W.E., 2008. Spectral signatures of characteristic spatial scales and nonfractal structure in landscapes. J. Geophys. Res. 113, F04003. http://dx.doi.org/10.1029/2007JF000866.
Power, W.L., Tullis, T.E., Weeks, J.D., 1988. Roughness and wear during brittle faulting. J. Geophys. Res. 93 (B12), 15268–15278.
Power, W.L., Tullis, T.E., 1991. Euclidean and fractal models for the description of rock surface-roughness. J. Geophys. Res. 96, 415–424.
Power, W.L., Tullis, T.E., Brown, S.R., Boitnott, G.N., Scholz, C.H., 1987. Roughness of natural fault surfaces. Geophys. Res. Lett. 14, 29–32.

Ran, Y.K., Fang, Z.J., Li, Z.Y., et al., 1992. Paleoseismicity and Segmentation along the Active Fault at the North Boundary of Huailai-zhuolu Basin, Hebei Province. Earthquake Research.
Ren, J.-W., Li, P., 1993. The characteristics of surface faulting of 1850 earthquake in Xichang, China. Seismology and Geology 15 (2), 97–106 (Chinese with English abstract).
Sagy, A., Brodsky, E.E., 2009. Geometric and rheological asperities in an exposed fault zone. J. Geophys. Res. 114, B02301. http://dx.doi.org/10.1029/2008JB005701.
Sagy, A., Brodsky, E.E., Axen, G.J., 2007. Evolution of fault-surface roughness with slip. Geology 35, 283–286.
Scholz, C.H., Avites, C.A., 1986. The fractal geometry of faults and faulting. In: Das, S., Boatwritht, J., Scholz, C. (Eds.), Earthquakes Source Mechanics, American Geophysical Union Monograph, vol. 37, pp. 147–156.
Scholz, C.H., 2002. The Mechanics of Earthquakes and Faulting. Cambridge University Press, Cambridge, New York, p. 496.
Simonsen, I., Hansen, A., Nes, O.M., 1998. Determination of the hurst exponent use of wavelet transforms. P. R. Enferm. 58, 2779–2787.
Smirrnova, T.Y., Nikonov, A.A., 1990. A revised lichenometric method and its application: dating past great past great earthquake. Arctic Alpine Res. 22, 375–388.
Stewart, I.S., 1993. In: Thomas, D.S.G., Allison, R.J. (Eds.), Sensitivity of Fault-generated Scarps as Indicators of Active Tectonism: Some Constrains from the Aegean Region, LandScape Sensitivity. Wiley, Chichester, pp. 129–147.
Stewart, I., 1996. A rough guide to limestone fault scarps. J. Struct. Geol. 18 (10), 1259–1264.
Wallace, R.E., 1984. Fault Scarps Formed during the Earthquake of October 2, 1915, Pleasant Valley, Nevada and Some Tectonic Implications. U.S.Geol.Surv. Prof., 1274-A.
Wang, G.C., Cao, K., Zhang, K.X., et al., 2011. Spatio-temporal framework of tectonic uplift stage of the Tibetan Plateau in Cenozoic. Sci. China: Earth Sci., 29–44.
Wei, Z.Y., He, H.L., Shi, F., Gao, X., Xu, C., 2010. Topographic characteristics of rupture surface associated with the 12 may 2008 Wenchuan earthquake. Bull. Seismol. Soc. Am. 100 (5B), 2669–2680.
Xu, X.W., Ma, X.Y., 1992. Neotectonic activity along the Shanxi rift system, China. Tectonophysics 219, 305–325.
Zreda, M.G., Noller, J., 1998. Ages of prehistoric earthquakes revealed by cosmogenic chlorine-36 in a bedrock fault scarp at Hebgen Lake. Science 292, 1097–1099.